Journal of Power Sources Advances 1 (2020) 100001

Contents lists available at ScienceDirect

Journal of Power Sources Advances

journal homepage: www.journals.elsevier.com/journal-of-power-sources-advances

Effect of PEM fuel cell porous media compression on in-plane transport phenomena

Mehdi Mortazavi [a,*], Anthony D. Santamaria [a], Vedang Chauhan [a], Jingru Z. Benner [a], Mahbod Heidari [b], Ezequiel F. Médici [c]

[a] Department of Mechanical Engineering, Western New England University, 1215 Wilbraham Road, Springfield, MA, 01119, USA
[b] Institute of Chemical Sciences and Engineering, Ecole Polytechnique Federale de Lausanne (EPFL), Lausanne, Switzerland
[c] Department of Mechanical Engineering-Engineering Mechanics, Michigan Technological University, 1400 Townsend Drive, Houghton, MI, 49931, USA

ARTICLE INFO

Keywords:
Gas diffusion layer (GDL)
Water transport
GDL compression
In-plane

ABSTRACT

Liquid-gas two-phase flow in the gas diffusion layer (GDL) of proton exchange membrane fuel cells is investigated using an ex-situ experimental setup. The mass transport phenomena is investigated in carbon paper and carbon cloth GDLs and at different compressions. Water percolation within the plane of the GDL is visualized with a CCD camera while its injection pressure is measured. Similarly, air percolation within the plane of GDL samples which were initially saturated with water is investigated. Experiments are conducted for the three flow regimes of stable displacement, capillary fingering, and viscous fingering. Images are analyzed to obtain the normalized wetted area. It is observed that while the GDL compression directly affects normalized wetted area for stable displacement and viscous fingering flow regimes, it has no impact on this parameter for capillary fingering flow regime. For stable displacement flow regime and for both carbon paper and carbon cloth samples, water percolation pressure increases with GDL compression. However, the water percolation pressure data obtained for capillary fingering flow regime does not suggest any discernible trend as a function of GDL compression. The findings in this study can be used to validate percolation models proposed by different schemes such as pore-network models.

1. Introduction

Proton exchange membrane (PEM) fuel cells are recognized as an alternative to internal combustion engines mainly because of their high volumetric power density and zero source greenhouse gas emissions [1–4]. During the operation of a PEM fuel cell, water is produced in the cathode side as a byproduct of the oxygen reduction reaction. This produced water may fill open pores of the gas diffusion layer (GDL) which threatens a uniform and continuous supply of reactant gases across the electrodes [5,6]. This can ultimately lower the performance of the cell due to high mass transfer overpotential [7–12]. Water transport through the porous structure of the PEM fuel cell electrode has been the subject of study for over a decade and a variety of hypotheses have been speculated on this regard. While some studies suggest that water transport by back diffusion from cathode to anode enhances when a micro-porous layer (MPL) is used [13–15], there are studies that suggest MPL has no impact on back diffusion [9,16-18]. Similarly, while there are studies that conclude the MPL enhances capillary-driven liquid water transport from the cathode catalyst layer to the cathode flow channel [19–24], a thoroughly opposite conclusion can also be found in literature [25]. In addition, there are some studies that suggest an enhanced vapor diffusion water transport from the cathode catalyst layer to the cathode flow channel as a consequence of coating GDLs with MPLs [26–28]. This uncertainty in water transport mechanism across the electrode is partially due to the uncertainty in water phase within the electrodes. In a recent study, Ge et al. [19] conducted an in situ, in operando, study on a PEM fuel cell by utilizing X-ray radiography to identify the phase of water as it transports within the electrode. By comparing the water content in the MPL and in vapor and liquid phases, they concluded that the liquid phase dominates. For an experiment conducted at 60°C, they reported that 92% of water transported through the MPL was in liquid phase. This value was 97% for an experiment conducted at 40°C. At the moment of breakthrough, defined as liquid water emergence from the opposite side of the MPL, the mean saturations of the MPL in the cathode side were reported to be 0.19 and 0.17 for operating temperatures of 60°C and 40°C, respectively. The higher water saturation at an elevated temperature was attributed to lower MPL capillary pressure. Therefore, a higher level of flooding in the cathode MPL was reported for a higher temperature

* Corresponding author.
E-mail address: mehdi.mortazavi@wne.edu (M. Mortazavi).

https://doi.org/10.1016/j.powera.2020.100001
Received 27 November 2019; Received in revised form 20 January 2020; Accepted 20 January 2020

gradient in the cathode MPL. Straubhaar et al. [29] studied water transport phase as it percolates through the GDL by using pore-network simulation featuring liquid-vapor phase change and suggested that the water transport could occurs in both liquid and vapor phases, depending on the stream-wise location from the channel inlet. For the region close to the inlet, their findings suggested that the GDL is relatively dry and the water transport could occur in vapor phase. Traveling in the stream-wise direction (close to the center of the channel), they suggested that water transport occurs by liquid invasion as well as evaporation-condensation. Finally, their pore-network model suggested that water transports in liquid phase in the region close to the channel outlet. The effect of temperature gradient was also investigated in their study and it was suggested that due to the temperature gradient across the electrode, water transport by vapor diffusion is a possibility. This vapor diffusion is accompanied by condensation within the GDL due to its lower temperature in flow channel side.

The mass transfer overpotential caused by the accumulation of liquid water in the porous electrode becomes the dominant limiting factor at high current densities where water production rate is high [30]. Water transport through the porous structure of the electrode is dominated by capillarity effects as the Bond number is less than unity [31]. The Bond number is a ratio of gravitational acceleration effects to surface tension effects on a liquid-vapor interface and is defined as $Bo = (L/L_c)^2$, where L and L_c are the characteristic length and capillary length, respectively. The characteristic length of the GDL is the mean pore radius which is in the order of 10–20 μm [32]. The capillary length is defined as $L_c = \sqrt{\sigma/\rho g}$, where σ is the surface tension, ρ is the liquid density, and g is the gravitational acceleration [31]. The small Bond number reflects the fact that water transport through the GDL is not dominated by gravitational effects. Instead, surface tension effects are dominant and influence the transport phenomena in PEM fuel cells. At the contact line region where a solid surface and two fluid phases are in contact, mechanical equilibrium can be attained if a pressure difference exists between the two fluids. This pressure difference, also referred to as the capillary pressure P_c, is defined by the Young-Laplace equation [33,34]:

$$P_c = 2\sigma H = \sigma \nabla \cdot \mathbf{n} \tag{1}$$

where H and **n** are the mean curvature of the separating surface and the unit vector normal to the surface, respectively. Therefore, the capillary pressure relevant to water transport within the GDL can be obtained by:

$$P_c = P_g - P_l = \frac{2\sigma cos\theta}{r} \tag{2}$$

where P_g, P_l, θ, and r are gas pressure, liquid pressure, water contact angle, and radius of the GDL pore, respectively. Because the capillary pressure is the pressure drop across the meniscus, the P_g and P_l in Eq. (2) will be the air pressure and the liquid water pressure, respectively, in this study. During the operation of a PEM fuel cell, the water produced in the catalyst layer must cross the GDL in vapor or liquid phase. The vapor can diffuse through the GDL pore. The liquid water accumulates behind the GDL with its pressure increasing until it surpasses the capillary pressure of the GDL. At this point, liquid water can intrude into the GDL. For transport within the GDL to continue the liquid water pressure must be greater than the GDL capillary pressure.

Water transport through the porous structure of the PEM fuel cell and within its flow channels has been extensively studied in literature [26,35–49]. In an early study done by Nam and Kaviany [22] the formation and distribution of condensed water in diffusion medium of PEM fuel cells was investigated. They suggested that liquid water transports from the catalyst layer to the gas channel in a branching-type geometry. In the transport model they suggested, water is transported from the catalyst layer to the gas channel through a main stream which is fed by smaller streams. Pasaogullari and Wang [10] later confirmed this model by developing a one-dimensional analytical model of water transport phenomena within the GDL. Litster et al. [38] visualized liquid water transport in the GDL by employing fluorescence microscopy techniques and suggested that water transport through the GDL is dominated by fingering and channeling, featuring numerous dead ends where water transport recedes when an adjacent breakthrough channel forms. Bazylak et al. [50] also utilized fluorescence microscopy to study liquid water transport through the GDL and described water emerges from the surface of the GDL at some specific locations referred to as *preferential* locations. They reported that these preferential locations change sporadically, an indication that water pathways are interconnected within the GDL. Gostick et al. [36,51] measured water saturation of the GDL at different capillary pressures and observed that water imbibition into a dry GDL and drainage from a water-saturated GDL is not spontaneous. Instead, the penetration of water and air into the GDL occurs when a positive displacement pressure is provided and water withdrawal is identified with negative capillary pressures. The latter was attributed to a network of hydrophilic pores within the GDL that were not covered by the polytetrafluoroethylene (PTFE) coating. As a common practice, GDLs are treated with PTFE in order to enhance water management [1,52,53]. Gostick et al. [36,51] also concluded that the main effect of treating GDL substrates with PTFE is to elevate the amount of work required to force water into the GDL while decreasing work required to withdraw water. Table 1 lists some of the studies done on transport phenomena in the porous structure of PEM fuel cells.

The GDL is the thickest porous layer used in PEM fuel cells with a thickness between 100 and 400 μm in contrast to the microporous layer (MPL) and catalyst layer with an average thicknesses of 30 and 15 μm, respectively. It is also more porous compared to the MPL and the catalyst layer. GDLs are of two types: carbon paper and carbon cloth, both consisting of carbon fibers. Carbon paper is obtained from randomly laced carbon fibers while carbon cloth is constructed of woven tows consisting of individual carbon fibers. Carbon papers are more porous compared to carbon clothes [54,55]. In addition, carbon clothes are spatially heterogeneous on a macroscopic scale while carbon papers are roughly spatially homogeneous. It has been reported by several authors that the GDL porosity decreases as the PTFE content in the GDL increases [13,25,56,57]. Fishman and Bazylak [58] took μCT images from PTFE treated GDLs and observed that due to PTFE treatment, local porosity of GDLs decreased near the surface region while PTFE was not evenly distributed throughout the substrates.

Liquid-gas two-phase flow in porous media is dominated by capillary and viscous effects with the two-phase distribution and flow regime being defined by the relative magnitude of each of these two effects. For instance, the viscous effect is negligible at low injection flow rate while the flow behavior is dominated by the capillary effect. If the intruding fluid is non-wetting the two-phase flow in the porous medium is designated as a drainage process. In contrast to the drainage process, the intrusion of a wetting fluid into the porous media is designated as an imbibition process. Therefore, transport of liquid water within the porous structure of the GDL is categorized under the drainage process. The drainage process may be in three different types of fluid flow, depending on the viscosity ratio as well as the capillary number. If the intruding fluid has a lower viscosity compared to the displaced fluid, viscous fingering occurs. The viscous fingering flow regime is characterized by irregular permeation of the injected fluid which results in a formation of multiple conduits or fingers. If the injected fluid has a viscosity greater than the viscosity of the displaced fluid either capillary fingering or stable displacement flow forms, depending on the injection flow rate. For low injection flow rates, capillary fingering occurs which is characterized by generation of irregular conduits within the porous medium. This flow regime includes few fingers of different sizes. For relatively high injection flow rate, the injected fluid permeates evenly within the porous layer which results in stable displacement flow distribution. The stable displacement flow regime does not include any finger formation. Instead, the injected fluid is percolating within the porous layer evenly in all directions. Lenormand et al. [59] proposed presenting these three flow

Table 1
Some of the studies done on transport phenomena in porous media of PEM fuel cells.

Author	Study	Approach	Direction
Williams et al. [61]	Characterized key properties affecting transport phenomena.	in-situ	through-plane
Ihonen et al. [55]	Measured the through-plane permeability of several materials.	in-situ	through-plane
Dai et al. [62]	Studied effects of PTFE content on water transport through the GDL.	in-situ	through-plane
Cho and Mench [63]	Described fundamentals of evaporative water removal during gas purge.	ex-situ	through-plane
Gostick et al. [64]	Measured permeability for a variety of samples. Also studied effects of GDL compression on permeability.	ex-situ	through-plane/in-plane
Gostick et al. [65]	Studied the breakthrough conditions in GDL.	ex-situ	through-plane
Fairweather et al. [66]	Studied effect of PTFE loading in GDL on water transport.	ex-situ	through-plane
Gostick et al. [36]	Studied the relationship of capillary pressure to liquid saturation.	ex-situ	through-plane
Nguyen et al. [67]	Measured capillary pressure in different GDL samples.	ex-situ	through-plane
Gallagher et al. [68]	Studied capillary pressure for different GDL saturation.	ex-situ	through-plane
Gostick et al. [51]	Measured capillary pressure at different saturation levels of a wetting phase.	ex-situ	through-plane
Hickner et al. [69]	High-resolution neutron radiography was used to image water content in the membrane electrode assembly and the gas flow channels.	in-situ	through-plane
Tamayol and Bahrami [70]	Investigated effects of GDL thickness and compression on water permeation.	ex-situ	through-plane
Owejan et al. [26]	Water vapor diffusion-drive and liquid-water pressure driven transport in porous layer was studied.	ex-situ/in-situ	through-plane
Daino et al. [71]	Studied water transport and temperature profile in anode and cathode side.	in-situ	through-plane
Litster et al. [38]	Fluorescence microscopy technique was employed to visualize water transport.	ex-situ	through-plane
Benziger et al. [72]	Positive capillary pressures were required to inject water into a GDL.	ex-situ	through-plane
Gao et al. [73]	Pore-scale visualizations of water in different types of GDLs were used to study transport phenomena in GDLs.	ex-situ	through-plane
Fairweather et al. [74]	Liquid water transport in GDL was studied by measuring the capillary pressure as a function of liquid water saturation.	ex-situ	through-plane
Harkness et al. [75]	Water transport through the GDL was studied by measuring capillary pressure.	ex-situ	through-plane
Liu and Pan [76]	Water transport through several commercial GDL substrates was studied.	ex-situ	through-plane
Koido et al. [77]	Proposed a series of analysis methods to identify the two-phase multi-component transport in the GDL.	ex-situ	through-plane
Kumbur et al. [78]	Capillary pressure as a function of liquid saturation was studied.	ex-situ	through-plane
Volfkovich et al. [79]	Water intrusion into GDLs with different PTFE loading was investigated.	ex-situ	through-plane
Lu et al. [80]	The liquid water breakthrough dynamics across GDLs was studied.	ex-situ	through-plane
Santamaria et al. [42]	Studied dynamic water transport by measuring capillary pressure.	ex-situ	through-plane
Médici and Allen [60]	Evaluated drainage phase diagram for GDL by studying water transport in GDL.	ex-situ	in-plane
Médici and Allen [81]	Studied transport phenomena in GDL samples and performed numerical simulation using a two-dimensional pore-network model.	ex-situ	in-plane
Médici and Allen [37]	Studied in-plane water transport in the GDL by suggesting a new scaling model in conjunction with the capillary number and the viscosity ratio.	ex-situ	in-plane
Stacy and Allen [82]	Measured the percolation pressure in catalyst layer.	ex-situ	in-plane
Alofari et al. [83]	Studied percolation in catalyst layer under controlled conditions.	ex-situ	in-plane
Mortazavi and Tajiri [84]	Studied liquid water transport through GDLs.	ex-situ	through-plane
Litster et al. [85]	Investigated water transport in a GDL by florescent imaging.	ex-situ	through-plane
Sinha et al. [86]	Quantified liquid water saturation distribution in GDLs by using X-ray microtomography.	ex-situ	in-plane
Yan et al. [87]	Investigated water balance in the porous structure of a PEM fuel cell by measurements the net drag coefficient.	ex-situ	through-plane
Zaffou et al. [88]	Investigated the effect of through-plane temperature difference on water transport.	ex-situ	through-plane
Bazylak et al. [89]	Studied transport phenomena by using fluorescence microscopy.	ex-situ	through-plane
Bazylak et al. [50]	The dynamic behavior of water transport through the GDL was investigated by fluorescence microscopy.	ex-situ	through-plane
Gostick et al. [35]	Water intrusion and removal from GDL samples was investigated by measuring capillary pressure at different GDL saturation.	ex-situ	through-plane
Kandlikar et al. [90]	Transport phenomena was investigated by measuring capillary pressure.	ex-situ	through-plane
Sinha et al. [91]	Proposed a pore-network model and a two-phase lattice Boltzmann model.	ex-situ	through-plane

regimes on a *drainages phase diagram*, as shown in Fig. 1c. The drainage phase diagram presents these flow regimes based on the capillary number, Ca, and the viscosity ratio, M:

$$\mathrm{Ca} = \frac{v\mu_{nw}}{\sigma} \tag{3}$$

$$\mathrm{M} = \frac{\mu_{nw}}{\mu_{w}} \tag{4}$$

where v, μ_{nw}, σ, and μ_{w} are the injected fluid velocity, the non-wetting fluid viscosity, surface tension, and the wetting fluid viscosity, respectively. The capillary number is a dimensionless number and is the ratio of viscous stress to capillary stress. Médici and Allen [60] showed the existence of the drainage phase diagram in PEM fuel cell GDL by exploring the three flow regimes of stable displacement, capillary fingering, and viscous fingering when the GDL was compressed by 20 kPa. However, because all experiments were conducted at a fixed compression, the effect of GDL compression on the transport phenomena was not identified. In this study, the three flow regimes are investigated for four different

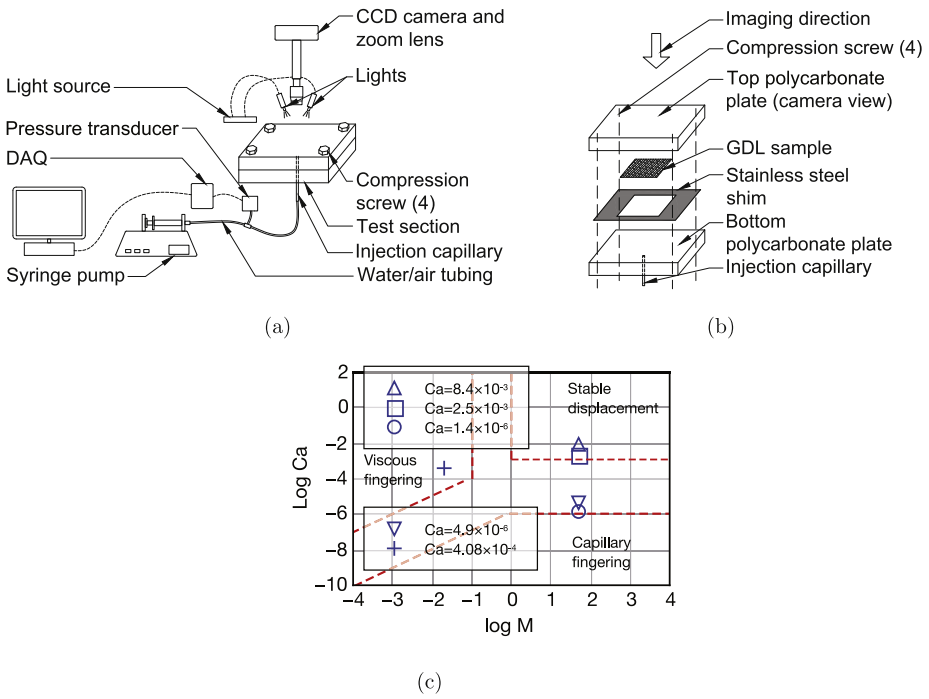

Fig. 1. a) Schematic of the experimental setup, b) schematic of the test section, and c) drainage phase diagram with flow conditions superimposed.

GDL compressions.

It can be concluded from Table 1 that most of the studies done on transport phenomena in the GDL are through-plane in direction while less attention has been paid to the in-plane direction. In this study, the three flow regimes of stable displacement, capillary fingering, and viscous fingering are investigated in carbon papers and carbon clothes as a function of GDL compression. While mass transport phenomena by stable displacement and viscous fingering do not occur in the porous structure of PEM fuel cells, evaluating all three percolation regimes in the GDL is still required for characterization and potential model validation beyond the PEM fuel cell operating conditions. Médici and Allen [37] proposed a scaling scheme for the dynamics of fluid percolation in thin porous layers and in conjunction with the capillary number and the viscosity ratio. Their proposed scaling scheme suggests a linear non-dimensional correlation between the saturation and the percolation pressure, regardless of the flow regime. In another study, Médici et al. [92] coupled the continuum and pore-network models to obtain liquid water distribution profiles across the GDL. The results presented in the current study could be used to validate models like those suggested by Médici and colleagues. Examples of other applications where these results could be used for include redox flow battery [93], direct borohydride fuel cells [94], and paper-based microfluidic diagnostics for medical diagnostics [95]. In this study the transport phenomena is investigated by visualizing the evolution of the injected fluid area as well as measuring percolation pressure with an ex-situ approach. Air or water percolation images are analyzed with an in-house-developed code to obtain the area occupied by the intruding fluid during percolation.

2. Experimental setup

2.1. Experimental setup

Fig. 1a shows the schematic of the experimental setup used in this study. For each run, an untreated 5-cm × 5-cm GDL sample was sandwiched between two 0.5-inch-thick polycarbonate plates and liquid water or air was injected from the bottom side of the test section with a syringe pump. For capillary fingering and stable displacement experiments water was injected through a 250-μm-diameter stainless steel capillary (U-111, Upchurch) and for viscous fingering experiments air was supplied through a 1.6-mm-diameter tube. Water and air percolations were visualized with a CCD camera (Thorlabs, 1501M-USB) from the top side of the test section. The camera was equipped with a zoom lens (Thorlabs, MVL6X12Z) and a 0.67X adapter (Thorlabs, MVL067A) to provide around 880 × 880 pixels over 5 cm × 5 cm cuts of the GDL sample, equivalent to 56.8 μm/pixel spatial resolution. Two different pressure transducers measured water pressure during the percolation within the GDL. The pressure transducer used for stable displacement experiments had a pressure range up to 103.0 kPa ± 0.3% (Omega, PX 481A-015G5V) and the pressure transducer used for capillary fingering experiments had a pressure range up to 11.7 kPa ± 1.0% (Omega, PX163-120BD5V). Four screws, one in each corner of the test section, provided the necessary compression which was controlled with 18-8 stainless steel shims at four different thicknesses. The shims surrounded the GDL samples within the test section as schematically shown in Fig. 1b. The four shim thicknesses used were 0.025, 0.050, 0.100, and 0.150 mm. The GDL carbon paper used was Toray TGP-060 with a manufacturer-specified thickness and porosity of 190 μm and 76%, respectively. The GDL carbon cloth used was AvCarb™ 1071 HCB with a thickness of 356 μm and a weave count-fill of 18.5 per cm. In this study, the GDL compression, λ, is defined by:

$$\lambda = \left(1 - \frac{\delta_{shim}}{\delta_{original}}\right) \times 100\% \quad (5)$$

where δ_{shim} and $\delta_{original}$ are the shim thickness and the thickness of the uncompressed GDL, respectively. Table 2 lists the GDL compression values, as defined in Eq. (5), for both GDL samples and by using different shim thicknesses.

2.2. Image processing

During each experiment, percolation images and pressures were recorded. The images from the CCD camera were analyzed to obtain the area occupied by the injected fluid. The water percolation images were captured at 12 frames per second. Images were processed with an in-house-developed MATLAB code by applying image filtering,

Table 2
GDL compressions calculated based on Eq. 5

GDL	Manufacturer-specified thickness (μm)	Shim thickness (mm)	λ (Eq. (5))
Toray TGP-060 (carbon paper)	190	0.025	86.84%
Toray TGP-060 (carbon paper)	190	0.050	73.68%
Toray TGP-060 (carbon paper)	190	0.100	47.36%
Toray TGP-060 (carbon paper)	190	0.150	21.05%
AvCarb™ 1071 HCB (carbon cloth)	356	0.025	92.97%
AvCarb™ 1071 HCB (carbon cloth)	356	0.050	85.95%
AvCarb™ 1071 HCB (carbon cloth)	356	0.100	71.91%
AvCarb™ 1071 HCB (carbon cloth)	356	0.150	57.86%

segmentation using thresholding, and connected component analysis via computer vision techniques. The image processing started by creating a mask image from the GDL substrate which featured the background details as black pixels. The next step include subtracting the background to remove the stationary details from the image. In addition, a noise removal procedure was done to remove any noise created from slight change in illumination, minor workbench vibrations, and motion blur. The obtained image was then transformed into a binary black and white image by applying thresholding. The binary black and white images were then analyzed to obtain the total number of white pixels which represent the percolation area in the GDL sample.

2.3. Flow condition

Table 3 lists experimental conditions used in this study. For stable displacement and capillary fingering flow regimes, the viscosity of the injected fluid should be greater than the viscosity of the displaced fluid. Therefore, water was injected to dry GDL samples. For viscous fingering experiments, the viscosity of injected fluid should be less than the viscosity of the displaced liquid. Therefore, air was injected into GDL samples which were initially saturated with liquid water. The velocity in the capillary number equation (Eq. (3)) was the fluid average velocity in the stainless steel capillary, $v = q/\pi r^2$, where v and q are the fluid average velocity and the volumetric flow rate, respectively. The flow conditions are shown in Fig. 1c based on the capillary number, Ca, and the viscosity ratio, M.

3. Results and discussion

3.1. Stable displacement

For Ca numbers greater than 10^{-3} and viscosity ratios greater than one, the drainage flow regime is stable displacement. In this flow regime, percolation starts from the center of the GDL sample, where the injection capillary is located, and water percolates within the GDL in a circular shape concentric to the injection hole, as shown in Figs. S1 and S2 in the supporting document. The non-dimensional time in these figures, t^*, is defined as

$$t^* = \frac{\text{time corresponding to image}}{\text{experiment duration}} \tag{6}$$

Fig. 2 shows normalized wetted area, A^*, as well as water percolation pressure for two water injection flow rates of 1×10^{-2} and 3.33×10^{-2} mℓ/s corresponding to Ca numbers of 2.5×10^{-3} and 8.4×10^{-3}, respectively. The normalized wetted area is defined as:

$$A^* = \frac{A_{injected}}{W \times L} \tag{7}$$

where $A_{injected}$, W, L, are the area occupied by the injected fluid, width of the GDL sample, and the length of the GDL sample, respectively. Experiments were continued until water reached edge of the GDL samples.

It can be observed from Fig. 2a that the normalized wetted area is affected by the shim thickness and therefore, the GDL compression. For the highest GDL compression which is obtained by the thinnest shim thickness (0.025 mm) the wetted area grows faster with respect to time compared to the other three shim thicknesses. This is due to smaller pore volume within the GDL samples at higher compressions which should be compensated by larger liquid area to accommodate the same volume of injected water at a given time. Fig. 2a suggests as the GDL gets more compressed, its normalized wetted area transforms from a linear trend to polynomials with larger curvatures. However, as time goes on the normalized wetted area drops off to a norm which is consistent with the curves for other GDL compressions. For the case of the least GDL compression corresponding to shim thickness 0.150 mm, the wetted area increases monotonically while for the highest GDL compression corresponding to shim thickness 0.025 mm, the normalized wetted area shows its highest curvature in this figure. A similar observation is made in Fig. 2b which shows normalized wetted area for water injection rate 3.33×10^{-2} mℓ/s corresponding to Ca number 2.5×10^{-3}. This observation can be explained by the change in GDL porosity at different compressions. Assuming that the volume of fibers remains constant at different compression values, the porosity of the compressed GDL can be calculated by:

$$\varepsilon_{new} = 1 - \left(1 - \varepsilon_{original}\right)\frac{\delta_{original}}{\delta_{new}} \tag{8}$$

where ε_{new}, $\varepsilon_{original}$, and δ_{new} are the porosity of compressed GDL, the porosity of uncompressed GDL, and the thickness of compressed GDL, respectively. $\delta_{original}$ is the thickness of uncompressed GDL as defined earlier. As more compression is applied on the GDL, $\delta_{original}/\delta_{new}$ increases and therefore the porosity of the compressed GDL, ε_{new}, decreases. Holzer et al. [96] performed X-ray tomographic microscopy of GDLs at different compressions and reported that the porosity decreases as the GDL compression increases. A comparison between Fig. 2a and b suggests a faster water percolation at a higher water flow rate which also results in larger injection area. Fig. 2c shows water pressure as it percolates within the plane of the GDL. It can be observed from this figure that pressure profiles are almost identical at the beginning of percolations but they deviate after a while. The figure also shows that water pressure increases with the GDL compression. This is attributed to smaller pore diameter at higher compressions which according to Eq. (2) increases the capillary pressure required to percolate within the GDL. The same trend in pressure is observed in Fig. 2d which shows water percolation pressures when water was injected at 3.33×10^{-2} mℓ/s. The only exception is the percolation pressure corresponding to 0.150 mm shim thickness which is slightly greater than the 0.100 mm shim thickness. The overall observation from Fig. 2c and d suggests a higher percolation pressure at higher water injection flow rate.

Fig. 3 shows the normalized wetted area and percolation pressure for stable displacement and in carbon cloth samples. The normalized wetted

Table 3
Experimental conditions.

Regime	Injected/displaced	M	q (mℓ/s)	Ca
Stable displacement	Water/air	48.90	1.00×10^{-2}	2.5×10^{-3}
Stable displacement	Water/air	48.90	3.33×10^{-2}	8.4×10^{-3}
Capillary fingering	Water/air	48.90	5.55×10^{-6}	1.4×10^{-6}
Capillary fingering	Water/air	48.90	1.94×10^{-5}	4.9×10^{-6}
Viscous fingering	Air/water	0.02	3.49	4.9×10^{-4}

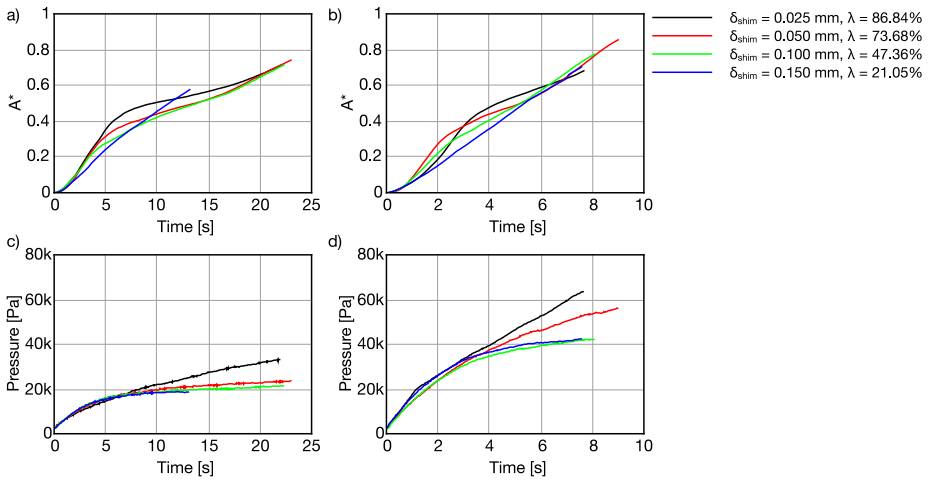

Fig. 2. Normalized wetted area (A*) and percolation pressure for stable displacement in carbon paper and at different GDL compressions, a and c) 1.00×10^{-2} mℓ/s

area for water flow rate 1.00×10^{-2} mℓ/s shown in Fig. 3a suggests an almost identical curve for the two thinnest shims used (0.025 and 0.050 mm). However, as the GDL compression decreases, this figure shows higher normalized wetted area, an observation which is in contrast to the one obtained from Fig. 2a and b. This can be explained by the pressure profile and the porosity of the carbon cloth samples. As shown in Fig. 3c, the percolation pressure increases with GDL compression, an observation which complies with Eq. (2) as well as Fig. 2c and d. Considering that the uncompressed carbon cloth used in this study was thicker than carbon paper samples (356 μm vs. 190 μm) and recalling that carbon clothes have lower porosity compared to carbon papers [54, 55], a high compression in carbon cloth samples transforms them into a barrier that resists water intrusion from the tip of the injection capillary. Therefore, water accumulates within the injection tube with its pressure increasing. The pressure increases until it exceeds the capillary pressure of the compressed GDL and water penetrates into the GDL sample. However, because of the excess resistance from the GDL sample, water intrusion into the GDL is limited, as reflected by normalized wetted area. Therefore, less water intrudes into the carbon cloth samples at higher compressions. As GDL compression decreases by employing thicker shims, GDL resistance to accommodate water decreases because of the higher porosity. As a result, more water can intrude into the GDL at lower compressions and water pressure decreases as shown in Fig. 3c. While a similar observation is obtained for the higher water flow rate of 3.33×10^{-2} mℓ/s (Fig. 3b and d), the normalized wetted area curves are still close to each other, particularly for the three shim thicknesses of 0.050, 0.100, and 0.150 mm. The pressure profiles shown in Fig. 3d shows substantially higher pressure for the thinnest shim which is an indication of water accumulation in the injection tube by considering the lowest normalized area for this shim thickness as shown in Fig. 3b.

3.2. Capillary fingering

The capillary fingering drainage flow regime is obtained at low injection flow rates for the non-wetting fluid. In contrast to the stable displacement regime which is characterized by a uniform percolation of the injected fluid, the capillary fingering flow regime features formation of few irregular conduits of fingers within the porous media, as shown in Fig. S3 in the supporting document. Fig. 4a and b shows the normalized wetted area for the capillary fingering flow regime in carbon paper samples. For both water flow rates tested, no discernible trend can be observed as a function of GDL compression. For instance, while Fig. 4a shows the highest normalized area for the shim thickness 0.100 mm Fig. 4b shows the lowest normalized wetted area for the same shim thickness. This unrecognizable trend in normalized wetted area can be attributed to low water flow rate which does not provide enough volume of water to keep the meniscus moving continuously. Therefore, percolation subsides until water pressure exceeds the capillary pressure of the

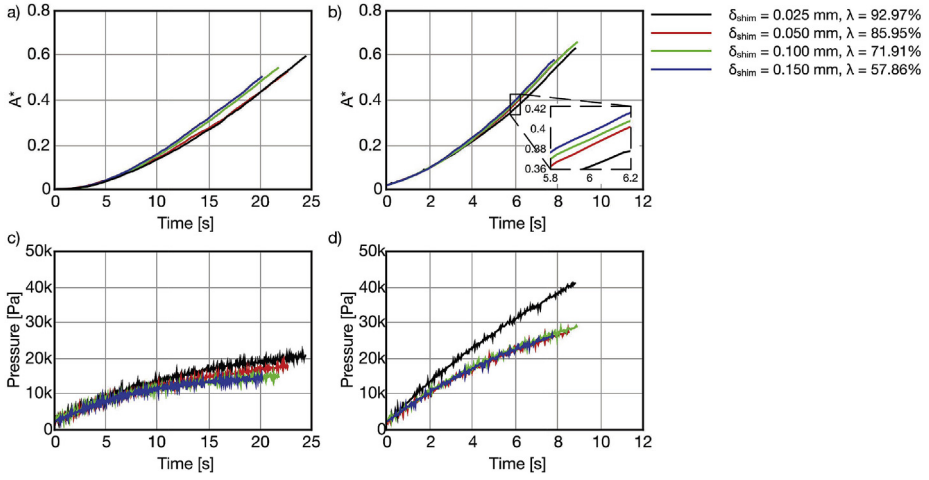

Fig. 3. Normalized wetted area (A*) and percolation pressure for stable displacement in carbon cloth and at different GDL compressions, a and c) 1.00×10^{-2} mℓ/s

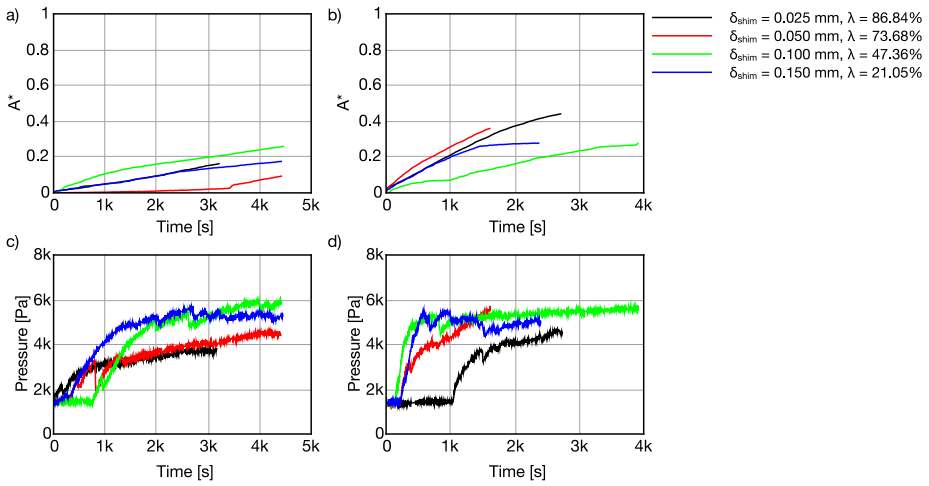

Fig. 4. Normalized wetted area (A^*) and percolation pressure for capillary fingering in carbon paper and at different GDL compressions, a and c) 5.55×10^{-6} mℓ/s,

porous layer. Percolation pressures for capillary fingering are shown in Fig. 4c and d. It can be observed from these figures that the pressure profiles gradually grow until they level off to a constant pressure between 4 and 6 kPa for both water flow rates tested. However, similar to normalized wetted area, no discernible trend can be detected in pressure profiles as a function of shim thickness.

3.3. Viscous fingering

The viscous fingering flow regime occurs when the injected fluid has lower viscosity compared to the displaced fluid. For these experiments, air was injected into GDL samples which were initially saturated with water by submerging them in deionized water for 12 h prior to the experiment. The viscous fingering flow regime features formation of multiple fingers of approximately an identical size. Fig. 5a shows normalized wetted area when air was injected to carbon paper samples and Fig. 5b shows normalized wetted area for carbon cloth samples. In both cases, air was injected at 3.49 mℓ/s. The normalized wetted area shown in this figure is the ratio of the GDL area occupied by air to the GDL sample area. It can be observed from this figure that the normalized wetted area increases with GDL compression both in carbon paper and carbon cloth experiments. According to Eq. (2), a higher gas pressure is required to displace water when the GDL pore radius, r, is small, a phenomenon that occurs at higher GDL compressions by thinner shims. This higher air pressure to displace water in a water-saturated GDL substrate is translated into a greater amount of work which should be provided by air, a conclusion which is in contrast to observations from Fig. 5. This discrepancy can be explained by the fact that as the GDL samples were squeezed in the test section, liquid water was removed from the samples and therefore, samples at higher compressions had lower water content at the beginning of the experiments. As a result, while air penetration into water-saturated GDL samples at higher compressions requires higher air pressure, because there is less water content in such GDLs, the normalized wetted area grows faster for experiments with thinner shims. For carbon paper results, the growth rate of the normalized area is evaluated for the first 5 s of each experiment. As shown in the inset of Fig. 5a, the normalized area curves were linearly fitted ($y = ax + b$) with the equations shown in different colors relevant to the shim thickness. The linear fit equations suggest that the greatest slope happens when the GDL is most compressed ($a = 0.111\ s^{-1}$). Except for the 0.050-mm-shim-thickness, the general trend observed in linear fit equations suggests a decrease in the linear fit slope as the GDL compression decreases. The only exception is the linear fit slope for the experiment with 0.050-mm-shim-thickness which is slightly lower than the linear fit slope for the experiment with 0.100 mm thick shim. However, the higher normalized area value after 5 s clearly indicates a higher growth rate for 0.050-mm-shim-thickness experiment compared to the 0.100-mm-shim-thickness experiment. The air pressure in viscous fingering experiments are not shown because of the rapid expansion of air which does not correspond to water displacement during viscous fingering experiments. This is because upon the initiation of the experiment, the high pressure air compressed in injection tubes expands rapidly which is accompanied by a fast growth of fingers. However, after the sudden air pressure drop liquid water still displaces while the air pressure has leveled off to its minimum value, an observation which was also reported by Médici and Allen [60]. While air pressure during its percolation in a water-saturated GDL sample has not been measured by any group so far, Gostick et al. [35] studied water intrusion to GDL and its withdrawal from the GDL by measuring capillary pressure and water saturation in Toray 090 carbon paper. They observed that water withdrawal began at $P_c \approx 5$ kPa and leveled off at $P_c \approx 15$ kPa. An application that could potentially use these viscous fingering results are interdigitated flow field design PEM fuel cells where liquid water could be expelled by convective transport, particularly under the land, when gas is purged [97]. Spernjak et al. [98] studied liquid water content in PEM fuel cell flow channels with an interdigitated flow field design and observed that the liquid water content is reduced as the air flow rate increases. However, only the water content in flow channels was investigated and water removal from the porous electrode, which is classified under viscous fingering, was not identified.

4. Conclusion

The three flow regimes of stable displacement, capillary fingering, and viscous fingering in the GDL of PEM fuel cells were investigated for different GDL compressions. Air or liquid water was injected into GDL samples and their evolutions were visualized with a CCD camera. Images were analyzed to obtain the normalized wetted area, defined as the ratio of the injected fluid area to the area of the GDL sample. For water injection experiments corresponding to stable displacement and capillary fingering, water injection pressure was also measured during water percolation. Both carbon paper and carbon cloth samples were tested in this study. For stable displacement experiments with carbon papers, results suggested higher normalized wetted area at higher GDL compressions. However, the opposite was observed for carbon cloth experiments at stable displacement conditions. Such observations were attributed to the lower porosity of carbon clothes with respect to carbon papers as well as their greater thickness which eventually transforms carbon cloth samples to a barrier resisting water intrusion and transport at higher compressions. For capillary fingering experiments no discernible trend was observed in area and pressure data, mainly due to the low water flow

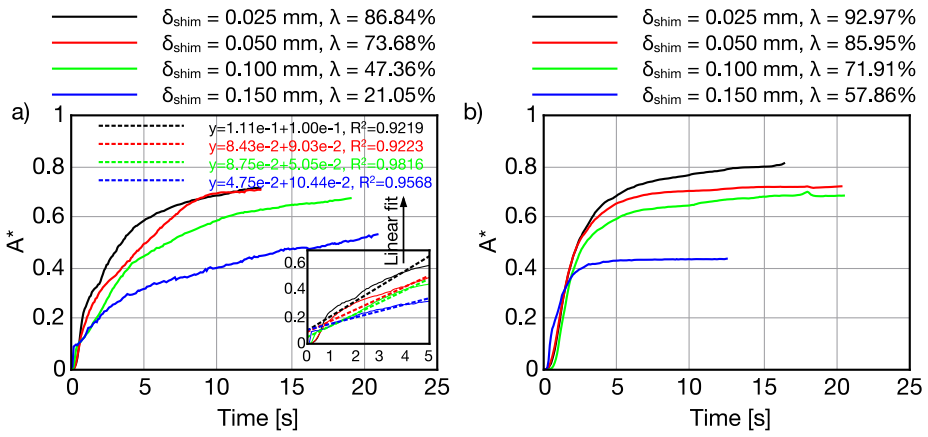

Fig. 5. Normalized wetted area (A^*) for viscous fingering at different GDL compressions, a) carbon paper with linear fit for the first 5 s as shown in the inset, and b) carbon cloth.

rate which does not provide enough volume of water to keep the meniscus moving continuously. For viscous fingering experiments, results suggested higher normalized wetted area at higher GDL compressions for carbon paper samples. This was attributed to less amount of water within GDL samples at higher compressions at the beginning of the experiments.

Declaration of competing interest

No potential conflict of interest was reported by the authors.

Acknowledgements

The Western New England University is gratefully acknowledged for financially supporting this study. The authors also would like to thank Peter Bennett for fabricating the test section used in this study.

Appendix A. Supplementary data

Supplementary data to this article can be found online at https://doi.org/10.1016/j.powera.2020.100001.

References

[1] H. Li, Y. Tang, Z. Wang, Z. Shi, S. Wu, D. Song, J. Zhang, K. Fatih, J. Zhang, H. Wang, et al., A review of water flooding issues in the proton exchange membrane fuel cell, J. Power Sources 178 (1) (2008) 103–117.
[2] M. Perry, T. Fuller, A historical perspective of fuel cell technology in the 20th century, J. Electrochem. Soc. 149 (2002) S59.
[3] A. Faghri, Z. Guo, Challenges and opportunities of thermal management issues related to fuel cell technology and modeling, Int. J. Heat Mass Tran. 48 (19) (2005) 3891–3920.
[4] R. Borup, J. Meyers, B. Pivovar, Y. Kim, R. Mukundan, N. Garland, D. Myers, M. Wilson, F. Garzon, D. Wood, et al., Scientific aspects of polymer electrolyte fuel cell durability and degradation, Chem. Rev. 107 (10) (2007) 3904–3951.
[5] H. Tang, A. Santamaria, J. Kurniawan, J.W. Park, T.-H. Yang, Y.-J. Sohn, Developing a 3d neutron tomography method for proton exchange membrane fuel cells, J. Power Sources 195 (19) (2010) 6774–6781.
[6] H. Tang, A. Santamaria, J.W. Park, C. Lee, W. Hwang, Quantification of water in hydrophobic and hydrophilic flow channels subjected to gas purging via neutron imaging, J. Power Sources 196 (22) (2011) 9373–9381.
[7] W. He, G. Lin, T. Van Nguyen, Diagnostic tool to detect electrode flooding in proton-exchange-membrane fuel cells, AIChE J. 49 (12) (2003) 3221–3228.
[8] J. Stumper, S.A. Campbell, D.P. Wilkinson, M.C. Johnson, M. Davis, In-situ methods for the determination of current distributions in PEM fuel cells, Electrochim. Acta 43 (1998) 3773–3783.
[9] D. Malevich, E. Halliop, B.A. Peppley, J.G. Pharoah, K. Karan, Investigation of charge-transfer and mass-transport resistances in PEMFCs with microporous layer using electrochemical impedance spectroscopy, J. Electrochem. Soc. 156 (2) (2009) B216–B224.
[10] U. Pasaogullari, C. Wang, Liquid water transport in gas diffusion layer of polymer electrolyte fuel cells, J. Electrochem. Soc. 151 (2004) A399.
[11] C.S. Kong, D. Kim, H. Lee, Y. Shul, T. Lee, Influence of pore-size distribution of diffusion layer on mass-transport problems of proton exchange membrane fuel cells, J. Power Sources 108 (1–2) (2002) 185–191.
[12] J. Bachman, M. Charvet, A. Santamaria, H.-Y. Tang, J.W. Park, R. Walker, Experimental investigation of the effect of channel length on performance and water accumulation in a PEMFC parallel flow field, Int. J. Hydrogen Energy 37 (22) (2012) 17 172–17 179.
[13] G. Lin, T. Van Nguyen, Effect of thickness and hydrophobic polymer content of the gas diffusion layer on electrode flooding level in a PEMFC, J. Electrochem. Soc. 152 (2005) A1942.
[14] D. Spernjak, A. Prasad, S. Advani, Experimental investigation of liquid water formation and transport in a transparent single-serpentine pem fuel cell, J. Power Sources 170 (2) (2007) 334–344.
[15] A. Weber, J. Newman, Effects of microporous layers in polymer electrolyte fuel cells, J. Electrochem. Soc. 152 (2005) A677.
[16] J.G. Pharoah, B. Peppley, H. Atiyeh, E. Halliop, K. Karan, A. Phoenix, Investigating the role of a microporous layer on the water transport and performance of a pemfc, ECS Transactions 3 (1) (2006) 1227–1237.
[17] K. Karan, H. Atiyeh, A. Phoenix, E. Halliop, J. Pharoah, B. Peppley, An experimental investigation of water transport in pemfcs, Electrochem. Solid State Lett. 10 (2007) B34.
[18] H. Atiyeh, K. Karan, B. Peppley, A. Phoenix, E. Halliop, J. Pharoah, Experimental investigation of the role of a microporous layer on the water transport and performance of a pem fuel cell, J. Power Sources 170 (1) (2007) 111–121.
[19] N. Ge, S. Chevalier, J. Lee, R. Yip, R. Banerjee, M.G. George, H. Liu, C. Lee, M. Fazeli, P. Antonacci, et al., Non-isothermal two-phase transport in a polymer electrolyte membrane fuel cell with crack-free microporous layers, Int. J. Heat Mass Tran. 107 (2017) 418–431.
[20] J. Lee, R. Yip, P. Antonacci, N. Ge, T. Kotaka, Y. Tabuchi, A. Bazylak, Synchrotron investigation of microporous layer thickness on liquid water distribution in a pem fuel cell, J. Electrochem. Soc. 162 (7) (2015) F669–F676.
[21] Y. Ji, G. Luo, C.-Y. Wang, Pore-level liquid water transport through composite diffusion media of pemfc, J. Electrochem. Soc. 157 (12) (2010) B1753–B1761.
[22] J. Nam, M. Kaviany, Effective diffusivity and water-saturation distribution in single- and two-layer PEMFC diffusion medium, Int. J. Heat Mass Tran. 46 (24) (2003) 4595–4611.
[23] U. Pasaogullari, C.-Y. Wang, K.S. Chen, Two-phase transport in polymer electrolyte fuel cells with bilayer cathode gas diffusion media, J. Electrochem. Soc. 152 (8) (2005) A1574–A1582.
[24] U. Pasaogullari, C.-Y. Wang, Two-phase transport and the role of micro-porous layer in polymer electrolyte fuel cells, Electrochim. Acta 49 (25) (2004) 4359–4369.
[25] G. Park, Y. Sohn, T. Yang, Y. Yoon, W. Lee, C. Kim, Effect of PTFE contents in the gas diffusion media on the performance of PEMFC, J. Power Sources 131 (1–2) (2004) 182–187.
[26] J. Owejan, J. Owejan, W. Gu, T. Trabold, T. Tighe, M. Mathias, Water transport mechanisms in PEMFC gas diffusion layers, J. Electrochem. Soc. 157 (2010) B1456.
[27] S.G. Kandlikar, Z. Lu, "Thermal management issues in a pemfc stack–a brief review of current status, Appl. Therm. Eng. 29 (7) (2009) 1276–1280.
[28] A. Thomas, G. Maranzana, S. Didierjean, J. Dillet, O. Lottin, Thermal and water transfer in pemfcs: investigating the role of the microporous layer, Int. J. Hydrogen Energy 39 (6) (2014) 2649–2658.
[29] B. Straubhaar, J. Pauchet, M. Prat, Water transport in gas diffusion layer of a polymer electrolyte fuel cell in the presence of a temperature gradient. phase change effect, Int. J. Hydrogen Energy 40 (35) (2015) 11668–11675.
[30] E. Ticianelli, C. Derouin, A. Redondo, S. Srinivasan, Methods to advance technology of proton exchange membrane fuel cells, J. Electrochem. Soc. 135 (1988) 2209.
[31] J. Allen, S. Son, S. Collicot, Proton exchange membrane fuel cell flow field design for improved water management, Handbook of Fuel Cells (2010) 1–12.
[32] M. Mortazavi, K. Tajiri, In-plane microstructure of gas diffusion layers with different properties for PEFC, J. Fuel Cell Sci. Technol. 11 (2) (2014), 021002.
[33] R. Defay, I. Prigogine, Surface Tension and Adsorption, Wiley, 1966.

[34] F. Dullien, Porous Media: Fluid Transport and Pore Structure, Academic Press, 1992.
[35] J. Gostick, M. Ioannidis, M. Fowler, M. Pritzker, Direct measurement of the capillary pressure characteristics of water–air–gas diffusion layer systems for PEM fuel cells, Electrochem. Commun. 10 (10) (2008) 1520–1523.
[36] J.T. Gostick, M.A. Ioannidis, M.W. Fowler, M.D. Pritzker, Wettability and capillary behavior of fibrous gas diffusion media for polymer electrolyte membrane fuel cells, J. Power Sources 194 (1) (2009) 433–444.
[37] E. Medici, J. Allen, Scaling percolation in thin porous layers, Phys. Fluids 23 (12) (2011) 122107.
[38] S. Litster, D. Sinton, N. Djilali, Ex situ visualization of liquid water transport in PEM fuel cell gas diffusion layers, J. Power Sources 154 (1) (2006) 95–105.
[39] I.V. Zenyuk, D.Y. Parkinson, G. Hwang, A.Z. Weber, Probing water distribution in compressed fuel-cell gas-diffusion layers using x-ray computed tomography, Electrochem. Commun. 53 (2015) 24–28.
[40] I.V. Zenyuk, A. Lamibrac, J. Eller, D.Y. Parkinson, F. Marone, F.N. Buchi, A.Z. Weber, Investigating evaporation in gas diffusion layers for fuel cells with x-ray computed tomography, J. Phys. Chem. C 120 (50) (2016), pp. 28 701–728 711.
[41] K. Jiao, J. Park, X. Li, Experimental investigations on liquid water removal from the gas diffusion layer by reactant flow in a PEM fuel cell, Appl. Energy 87 (9) (2010) 2770–2777.
[42] A.D. Santamaria, P.K. Das, J.C. MacDonald, A.Z. Weber, Liquid-water interactions with gas-diffusion-layer surfaces, J. Electrochem. Soc. 161 (12) (2014) F1184–F1193.
[43] J. Park, H. Oh, Y.I. Lee, K. Min, E. Lee, J.-Y. Jyoung, Effect of the pore size variation in the substrate of the gas diffusion layer on water management and fuel cell performance, Appl. Energy 171 (2016) 200–212.
[44] M. Mortazavi, K. Tajiri, Two-phase flow pressure drop in flow channels of proton exchange membrane fuel cells: review of experimental approaches, Renew. Sustain. Energy Rev. 45 (2015) 296–317.
[45] P.K. Das, X. Li, Z.-S. Liu, Effective transport coefficients in PEM fuel cell catalyst and gas diffusion layers: beyond bruggeman approximation, Appl. Energy 87 (9) (2010) 2785–2796.
[46] M. Mortazavi, M. Heidari, S.A. Niknam, "A discussion about two-phase flow pressure drop in proton exchange membrane fuel cells, Heat Tran. Eng. (2019) 1–16, https://doi.org/10.1080/01457632.2019.1670460.
[47] M. Mortazavi, A.D. Santamaria, J.Z. Benner, V. Chauhan, Enhanced water removal from PEM fuel cells using acoustic pressure waves, J. Electrochem. Soc. 166 (7) (2019) F3143–F3153.
[48] H. Tang, A.D. Santamaria, J. Bachman, J.W. Park, Vacuum-assisted drying of polymer electrolyte membrane fuel cell, Appl. Energy 107 (2013) 264–270.
[49] S.A. Niknam, M. Mortazavi, A.D. Santamaria, Signature analysis of two-phase flow pressure drop in proton exchange membrane fuel cell flow channels, Results in Engineering (2019) 100071, https://doi.org/10.1016/j.rineng.2019.100071.
[50] A. Bazylak, D. Sinton, N. Djilali, Dynamic water transport and droplet emergence in PEMFC gas diffusion layers, J. Power Sources 176 (1) (2008) 240–246.
[51] J. Gostick, M. Fowler, M. Ioannidis, M. Pritzker, Y. Volfkovich, A. Sakars, Capillary pressure and hydrophilic porosity in gas diffusion layers for polymer electrolyte fuel cells, J. Power Sources 156 (2) (2006) 375–387.
[52] M. Mathias, J. Roth, J. Fleming, W. Lehnert, Handbook of Fuel Cells-Fundamentals, Technology and Applications, Vol. 3: Fuel Cell Technology and Application, *John Wiley & Sons, NY*, 2003, pp. 517–537.
[53] M. Mortazavi, K. Tajiri, Effect of the PTFE content in the gas diffusion layer on water transport in polymer electrolyte fuel cells (PEFCs), J. Power Sources 245 (2014) 236–244.
[54] M. Mathias, J. Roth, J. Fleming, W. Lehnert, Diffusion media materials and characterisation, Handbook of fuel cells (2010).
[55] J. Ihonen, M. Mikkola, G. Lindbergh, Flooding of gas diffusion backing in PEFCs physical and electrochemical characterization, J. Electrochem. Soc. 151 (8) (2004) A1152–A1161.
[56] S. Park, B. Popov, Effect of cathode GDL characteristics on mass transport in PEM fuel cells, Fuel 88 (11) (2009) 2068–2073.
[57] J. Lobato, P. Canizares, M. Rodrigo, C. Ruiz-López, J. Linares, Influence of the Teflon loading in the gas diffusion layer of PBI-based PEM fuel cells, J. Appl. Electrochem. 38 (6) (2008) 793–802.
[58] Z. Fishman, A. Bazylak, Heterogeneous through-plane porosity distributions for treated PEMFC GDLs I. PTFE effect, J. Electrochem. Soc. 158 (2011) B841.
[59] R. Lenormand, E. Touboul, C. Zarcone, Numerical models and experiments on immiscible displacements in porous media, J. Fluid Mech. 189 (1988) 165–187.
[60] E. Médici, J. Allen, Existence of the phase drainage diagram in proton exchange membrane fuel cell fibrous diffusion media, J. Power Sources 191 (2) (2009) 417–427.
[61] M. Williams, E. Begg, L. Bonville, H. Kunz, J. Fenton, Characterization of gas diffusion layers for PEMFC, J. Electrochem. Soc. 151 (2004) A1173.
[62] W. Dai, H. Wang, X. Yuan, J. Martin, J. Shen, M. Pan, Z. Luo, Measurement of water transport rates across the gas diffusion layer in a proton exchange membrane fuel cell, and the influence of polytetrafluoroethylene content and micro-porous layer, J. Power Sources 188 (1) (2009) 122–126.
[63] K. Cho, M. Mench, Effect of material properties on evaporative water removal from polymer electrolyte fuel cell diffusion media, J. Power Sources 195 (19) (2010) 6748–6757.
[64] J. Gostick, M. Fowler, M. Pritzker, M. Ioannidis, L. Behra, In-plane and through-plane gas permeability of carbon fiber electrode backing layers, J. Power Sources 162 (1) (2006) 228–238.
[65] J. Gostick, M. Ioannidis, M. Pritzker, M. Fowler, Impact of liquid water on reactant mass transfer in PEM fuel cell electrodes, J. Electrochem. Soc. 157 (2010) B563.
[66] J. Fairweather, P. Cheung, D. Schwartz, The effects of wetproofing on the capillary properties of proton exchange membrane fuel cell gas diffusion layers, J. Power Sources 195 (3) (2010) 787–793.
[67] T. Nguyen, G. Lin, H. Ohn, X. Wang, Measurement of capillary pressure property of gas diffusion media used in proton exchange membrane fuel cells, Electrochem. Solid State Lett. 11 (2008) B127.
[68] K. Gallagher, R. Darling, T. Patterson, M. Perry, Capillary pressure saturation relations for PEM fuel cell gas diffusion layers, J. Electrochem. Soc. 155 (2008) B1225.
[69] M. Hickner, N. Siegel, K. Chen, D. Hussey, D. Jacobson, M. Arif, In situ high-resolution neutron radiography of cross-sectional liquid water profiles in proton exchange membrane fuel cells, J. Electrochem. Soc. 155 (2008) B427.
[70] A. Tamayol, M. Bahrami, Water permeation through gas diffusion layers of proton exchange membrane fuel cells, J. Power Sources 196 (2011) 6356–6361.
[71] M. Daino, Z. Lu, J. LaManna, J. Owejan, T. Trabold, S. Kandlikar, Through-plane water transport visualization in a PEMFC by visible and infrared imaging, Electrochem. Solid State Lett. 14 (2011) B51.
[72] J. Benziger, J. Nehlsen, D. Blackwell, T. Brennan, J. Itescu, Water flow in the gas diffusion layer of PEM fuel cells, J. Membr. Sci. 261 (1–2) (2005) 98–106.
[73] B. Gao, T. Steenhuis, Y. Zevi, J. Parlange, R. Carter, T. Trabold, et al., Visualization of unstable water flow in a fuel cell gas diffusion layer, J. Power Sources 190 (2) (2009) 493–498.
[74] J. Fairweather, P. Cheung, J. St-Pierre, D. Schwartz, A microfluidic approach for measuring capillary pressure in PEMFC gas diffusion layers, Electrochem. Commun. 9 (9) (2007) 2340–2345.
[75] I. Harkness, N. Hussain, L. Smith, J. Sharman, The use of a novel water porosimeter to predict the water handling behaviour of gas diffusion media used in polymer electrolyte fuel cells, J. Power Sources 193 (1) (2009) 122–129.
[76] T. Liu, C. Pan, Visualization and back pressure analysis of water transport through gas diffusion layers of proton exchange membrane fuel cell, J. Power Sources 207 (2012) 60–69.
[77] T. Koido, T. Furusawa, K. Moriyama, An approach to modeling two-phase transport in the gas diffusion layer of a proton exchange membrane fuel cell, J. Power Sources 175 (1) (2008) 127–136.
[78] E. Kumbur, K. Sharp, M. Mench, Validated leverett approach for multiphase flow in PEFC diffusion media i. hydrophobicity effect, J. Electrochem. Soc. 154 (12) (2007) B1295–B1304.
[79] Y.M. Volfkovich, V. Sosenkin, N. Nikolskaya, T. Kulova, Porous structure and hydrophilic-hydrophobic properties of gas diffusion layers of the electrodes in proton-exchange membrane fuel cells, Russ. J. Electrochem. 44 (3) (2008) 278–285.
[80] Z. Lu, M.M. Daino, C. Rath, S.G. Kandlikar, Water management studies in PEM fuel cells, part III: dynamic breakthrough and intermittent drainage characteristics from GDLs with and without MPLs, Int. J. Hydrogen Energy 35 (9) (2010) 4222–4233.
[81] E.F. Médici, J.S. Allen, A quantitative technique to compare experimental observations and numerical simulations of percolation in thin porous materials, Transport Porous Media 115 (3) (2016) 435–447.
[82] S.A. Stacy, J.S. Allen, Percolation in a proton exchange membrane fuel cell catalyst layer, ECS Transactions 50 (2) (2013) 877–884.
[83] K.T. Alofari, E. Medici, K. Tajiri, J.S. Allen, Percolation behavior in catalytic porous material, ECS Transactions 92 (8) (2019) 71–76.
[84] M. Mortazavi, K. Tajiri, Liquid water breakthrough pressure through gas diffusion layer of proton exchange membrane fuel cell, Int. J. Hydrogen Energy 39 (17) (2014) 9409–9419.
[85] S. Litster, A. Bazylak, D. Sinton, N. Djilali, Water transport in gas diffusion layers of pemfcs, ECS Transactions 3 (1) (2006) 409–414.
[86] P. Sinha, P. Halleck, C. Wang, Quantification of liquid water saturation in a PEM fuel cell diffusion medium using X-ray microtomography, Electrochem. Solid State Lett. 9 (7) (2006) A344–A348.
[87] Q. Yan, H. Toghiani, J. Wu, Investigation of water transport through membrane in a PEM fuel cell by water balance experiments, J. Power Sources 158 (1) (2006) 316–325.
[88] R. Zaffou, S. Jung, H. Kunz, J. Fenton, Temperature-driven water transport through membrane electrode assembly of proton exchange membrane fuel cells, Electrochem. Solid State Lett. 9 (9) (2006) A418–A422.
[89] A. Bazylak, D. Sinton, Z. Liu, N. Djilali, Effect of compression on liquid water transport and microstructure of PEMFC gas diffusion layers, J. Power Sources 163 (2) (2007) 784–792.
[90] S. Kandlikar, M. Garofalo, Z. Lu, Water management in a PEMFC: water transport mechanism and material degradation in gas diffusion layers, Fuel Cell. 11 (2011) 814–823.
[91] P. Sinha, P. Mukherjee, C. Wang, Impact of gdl structure and wettability on water management in polymer electrolyte fuel cells, J. Mater. Chem. 17 (30) (2007) 3089–3103.
[92] E.F. Médici, I.V. Zenyuk, D. Parkinson, A. Weber, J. Allen, Understanding water transport in polymer electrolyte fuel cells using coupled continuum and pore-network models, Fuel Cell. 16 (6) (2016) 725–733.
[93] R. Banerjee, N. Bevilacqua, A. Mohseninia, B. Wiedemann, F. Wilhelm, J. Scholta, R. Zeis, Carbon felt electrodes for redox ow battery: impact of compression on transport properties, Journal of Energy Storage 26 (2019) 100997.
[94] L. An, C. Jung, Transport phenomena in direct borohydride fuel cells, Appl. Energy 205 (2017) 1270–1282.
[95] M.M. Gong, D. Sinton, Turning the page: advancing paper-based microuidics for broad diagnostic application, Chem. Rev. 117 (12) (2017) 8447–8480.
[96] L. Holzer, O. Pecho, J. Schumacher, P. Marmet, O. Stenzel, F. Büchi, A. Lamibrac, B. Münch, Microstructure-property relationships in a gas di_usion layer (gdl) for

polymer electrolyte fuel cells, part i: effect of compression and anisotropy of dry gdl, Electrochim. Acta 227 (2017) 419–434.

[97] A.D. Santamaria, M.K. Becton, N.J. Cooper, A.Z. Weber, J.W. Park, Effect of cross-ow on pefc liquid-water distribution: an in-situ high-resolution neutron radiography study, J. Power Sources 293 (2015) 162–169.

[98] D. Spernjak, A.K. Prasad, S.G. Advani, In situ comparison of water content and dynamics in parallel, single-serpentine, and interdigitated ow _elds of polymer electrolyte membrane fuel cells, J. Power Sources 195 (11) (2010) 3553–3568.